Earth and Planetary Science Letters 491 (2018) 11–20

Contents lists available at ScienceDirect

Earth and Planetary Science Letters

www.elsevier.com/locate/epsl

Bulk properties and near-critical behaviour of SiO_2 fluid

Eleanor C.R. Green [a,*], Emilio Artacho [b,c,d,e], James A.D. Connolly [a]

[a] Department of Earth Sciences, ETH Zurich, Clausiusstrasse 25, 8092 Zurich, Switzerland
[b] Theory of Condensed Matter, Cavendish Laboratory, University of Cambridge, Cambridge, CB3 0HE, UK
[c] CIC nanoGUNE, E-20018 Donostia-San Sebastián, Spain
[d] Basque Foundation for Science Ikerbasque, E-48011 Bilbao, Spain
[e] Donostia International Physics Center, E-20018 Donostia-San Sebastián, Spain

ARTICLE INFO

Article history:
Received 15 November 2017
Received in revised form 3 March 2018
Accepted 10 March 2018
Available online 27 March 2018
Editor: F. Moynier

Keywords:
silica
equation of state
critical point
depolymerisation
strong and fragile liquids

ABSTRACT

Rocky planets and satellites form through impact and accretion processes that often involve silicate fluids at extreme temperatures. First-principles molecular dynamics (FPMD) simulations have been used to investigate the bulk thermodynamic properties of SiO_2 fluid at high temperatures (4000–6000 K) and low densities (500–2240 kg m^{-3}), conditions which are relevant to protoplanetary disc condensation. Liquid SiO_2 is highly networked at the upper end of this density range, but depolymerises with increasing temperature and volume, in a process characterised by the formation of oxygen–oxygen (O=O) pairs. The onset of vaporisation is closely associated with the depolymerisation process, and is likely to be non-stoichiometric at high temperature, initiated via the exsolution of O_2 molecules to leave a Si-enriched fluid. By 6000 K the simulated fluid is supercritical. A large anomaly in the constant-volume heat capacity occurs near the critical temperature. We present tabulated thermodynamic properties for silica fluid that reconcile observations from FPMD simulations with current knowledge of the SiO_2 melting curve and experimental Hugoniot curves.

1. Introduction

Silica is the building block of the silicate minerals, and thus an Earth-forming material of fundamental importance. The Earth Sciences are usually concerned with silicates in the solid state, or the liquid state not far above the melting point, where the liquid density is similar to that of the solid. However, the formation of rocky exoplanets and satellites involves high-entropy proto-planetary or post-impact debris discs. To model silicate fluid in such a disc at high temperatures and low densities, it is necessary to estimate the critical point of the fluid, since it is only below the critical temperature that physical partitioning of vapour and liquid reservoirs can occur on cooling, with associated chemical fractionation (e.g. Pahlevan et al., 2011). For silica, often treated as a simple analogue for silicate systems, the critical point in temperature–density space is thought to be in the vicinity of 5000–6000 K, 500–700 kg m^{-3} (summarised in Connolly, 2016).

Under the high-temperature, low-density conditions of the predicted critical point, the properties of silica fluid are difficult to probe experimentally. By contrast, there is abundant experimental information in other parts of the stable fluid field. At 1 bar, both the melting point and boiling point are known, the latter with the aid of thermodynamic analysis (e.g. Kraus et al., 2012; Schick, 1960; Schnurre et al., 2004). Calorimetric and volumetric properties have been constrained (e.g. Lange and Carmichael, 1987; Stebbins et al., 1984), although, due to the exceptional viscosity of SiO_2 liquid, these values are usually extrapolated from measurements in multicomponent systems. The melting curve is known experimentally to $P \leq 120$ kbar, as summarised in the thermodynamic analysis of Holland and Powell (2011, see Supplementary Materials). Shock wave experiments have been used to trace SiO_2 Hugoniot curves into regions of temperature–density space accessible by giant impacts. Starting from, typically, α-quartz (2650 kg m^{-3}) or fused silica (2200 kg m^{-3}), such experiments have explored trajectories of 5×10^3–1×10^5 K, 4500–8000 kg m^{-3}, and 5×10^2–2×10^4 kbar (e.g. Hicks et al., 2005; Kraus et al., 2012; McCoy et al., 2016b). Along these trajectories, at temperatures in excess of 3×10^4 K, the fluid becomes a conductive plasma (Hicks et al., 2006). In recent years, the shock wave approach has been adapted for high-temperature, low-density conditions; using silica aerogel as a starting material, Knudson and Lemke (2013) and Falk et al. (2014) obtained shocked materials with densities of ~1100 kg m^{-3}, at 1×10^4–8×10^4 K and 300–2000 kbar. However, only the study of Kraus et al. (2012) directly investigated the

* Corresponding author.
E-mail addresses: eleanor.green@erdw.ethz.ch (E.C.R. Green), ea245@cam.ac.uk (E. Artacho), james.connolly@erdw.ethz.ch (J.A.D. Connolly).

https://doi.org/10.1016/j.epsl.2018.03.015
0012-821X/

products of post-shock decompression in the vicinity of the liquid–vapour critical point. Their work entailed complex measurements of density and models of entropy, based on the assumption that the post-shock material decompressed isentropically.

Molecular dynamics methods offer a valuable supplement to experiments, especially under experimentally challenging conditions. First-principles molecular dynamics (FPMD) under density functional theory (DFT) have been used to extend the experimental SiO_2 melting curve to conditions in excess of 5.5×10^4 kbar, 2×10^4 K (González-Cataldo et al., 2016; Usui and Tsuchiya, 2010). Qi et al. (2015) used FPMD to simulate the Hugoniot for silica with starting densities of up to 2940 kg m^{-3}. The studies of Karki et al. (2007), Kim et al. (2012), Sarnthein et al. (1995) and Trave et al. (2002) allow thermodynamic, structural and transport properties to be assessed for SiO_2 liquid over a temperature–density grid, at 300–6000 K and above 2100 kg m^{-3}, similar to the density at the 1 bar melting point. At lower densities but much higher temperatures (1000–1200 kg m^{-3}, 1×10^4–8×10^4 K), Falk et al. (2014) complemented their shock experiments with low-density DFT simulations, deep in the supercritical fluid field, while Karki et al. (2013) explored the viscosity of zero-pressure SiO_2 fluid at densities of 780–2180 kg m^{-3}. A further large body of work investigates liquid and glassy silica via empirical-potential molecular dynamics (EPMD). Horbach and Kob (1999), Lascaris et al. (2014) and Saika-Voivod et al. (2000) applied the pairwise potentials of van Beest et al. (1990) and Woodcock et al. (1976) to liquids with density of 2000 kg m^{-3} and above. Kieffer and Angell (1988) simulated aerogel-like amorphous silica, subject to isotropic tensile stress, with bulk densities of 100–1600 kg m^{-3} along a 300 K isotherm. EPMD allows larger sample sizes and longer simulation times than FPMD, and has suggested a number of insights, for example with respect to strong versus fragile behaviour of the silica liquid and its relation to thermodynamic properties (Angell and Hemmati, 2013). However, the computationally inexpensive pairwise potentials are associated with substantial errors in the absolute temperatures of phase phenomena (∼1000 K, e.g. Saika-Voivod et al., 2004).

There is a shortage of constraints on silica fluid at densities of 0–2000 kg m^{-3}, temperatures of 0–10^4 K and pressures of 0–5 kbar, the region thought to contain the critical point (e.g. Melosh, 2007). Notwithstanding, the importance of silica is such that numerous equations of state, encompassing the critical region, have been proposed for its solid and its fluid states. The hydrocode of Melosh for SiO_2 (Melosh, 2007) is a long-range thermodynamic equation of state (EoS), encompassing fluid and solid states, and is therefore suitable for impact modelling involving terrestrial planetary bodies. An equation of state for Mg–Si–O liquid in the Earth's mantle was presented by de Koker and Stixrude (2009), but has yet to be extrapolated to conditions of lower fluid density. Iosilevskiy et al. (2014) presented a range of preliminary EoS for SiO_2, and acknowledged the possibility that boiling is significantly incongruent at critical conditions, though at 1 bar it is essentially congruent (Schick, 1960). Connolly (2016) developed a van der Waal's style molecular EoS for Si–O fluids that explicitly allows for speciation and predicts slightly incongruent boiling of a bulk SiO_2 system. There is substantial overlap in the predictions of critical conditions derived from these models. However, apart from the analysis by Kraus et al. (2012) of post-decompression materials there are no independent constraints on the critical conditions, nor on the implied nature of the near-critical fluid.

The present study aims to clarify the nature of SiO_2 liquid at densities of 500–2240 kg m^{-3} and temperatures of 4000–6000 K, and gain insight into near-critical behaviour. The results are analysed in the context of melting curve and shock wave data. We illustrate this analysis by retabulating the hydrocode output of Melosh (2007) in the stable fluid region.

2. Methods

Simulations were carried out under density functional theory using the SIESTA ab initio package (Soler et al., 2002). The generalised gradient approximation (GGA; Perdew et al., 1996) was used to account for the energy of exchange and correlation among the electrons. Simulations took place in the microcanonical (NVE) ensemble, at densities of 499–2237 kg m^{-3}, and nominal temperatures of 4000–6000 K. True ensemble average temperatures are given in Table S1 of the Supplementary Materials. The cubic simulation box contained 24 SiO_2 units (72 atoms), repeated periodically. At lower, near-critical densities, the small systems accessible in DFT are unable to undergo phase separation, due to the dominance of the free energy penalty associated with interfaces. Nevertheless, in the DFT system of this study, trends in bulk properties distinguish stable one-phase regions from regions of inhibited phase separation. Section S1 of the Supplementary Materials discusses the methodology in full.

3. Direct observations of critical behaviour from pressure–volume isotherms

Bulk properties obtained in production runs are presented in Table S1, along with the properties of three low-density simulations at 4000 K that were annealed with no true production runs (Supplementary Materials section S1). The results are shown in pressure–volume (P–V) space (Fig. 1a), with isotherms sketched at 4000, 5000 and 6000 K. At volumes beyond the range of the simulations, 6000 K isotherms are shown for hypothetical ideal silica vapours consisting of SiO_2 and $SiO + ½O_2$. This allows the simulation results to be compared with the expected geometry of isotherms for a fluid in its liquid, gaseous and transitional states (Figs. 1b and 1c).

By comparison with the theoretical curves in P–V space, simulated isotherms appear to describe (i) a liquid region at <80 Å per SiO_2 unit (1250 kg m^{-3}), with large, negative $\partial P/\partial V$, (ii) a region of much lower-gradient, more vapour-like isotherms at volumes >80 Å, that plausibly represents the two-phase field of liquid–vapour coexistence (shown as dashed lines in Fig. 1a), and (iii) a supercritical fluid represented by the 6000 K isotherm, along which $\partial P/\partial V$ is consistently negative.

The 6000 K isotherm provides an upper limit on the critical temperature and pressure. Simulations on this isotherm at 150.0 Å (665 kg m^{-3}) and 200.0 Å (499 kg m^{-3}) showed exceptional fluctuations in the partitioning of kinetic and potential energy, superimposed on the thermal fluctuations, as expected close to a critical point. Of the three simulated isotherms, the 5000 K isotherm is the most difficult to interpret, given the low resolution of the simulations in P–V space. It is assumed to be just-subcritical, on the grounds that it is almost pressure-independent at 100–200 Å (1000–4800 kg m^{-3}). The simulation at 5000 K and 200.0 Å (499 kg m^{-3}) showed large fluctuations as described above for 6000 K. The 4000 K isotherm is unambiguously subcritical. From low to high volume along this isotherm, the liquid state is stable at 44.6 Å (2237 kg m^{-3}), and metastable when it is in tension at $P < 0$. A point must exist, between the (4000 K, 44.6 Å) coordinate and the intersection of the 4000 K isotherm with $P = 0$, at which the liquid first becomes metastable with respect to a two-phase liquid–vapour field. Simulations at 4000 K and 99.8–200.0 Å did not involve a production run, but suggest an isotherm geometry that is qualitatively consistent with the theoretical isotherm of an unstable 1-phase fluid inside the spinodal curve (indicated by the red and dashed grey curves in Fig. 1c). Such behaviour

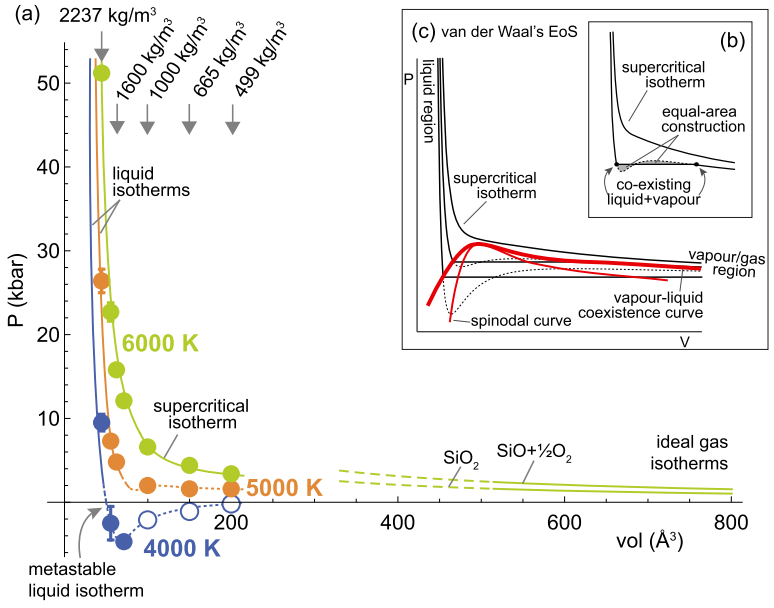

Fig. 1. (a) Pressure versus volume obtained in simulations using GGA. Simulations without production runs are shown as white circles. Isotherms are sketched at 4000 K (blue), 5000 K (orange) and 6000 K (green), and interpreted based on their geometries. Dotted curves indicate metastable or unstable (inter-spinodal) isotherms, where phase separation would take place in a system of infinite extent. Dashed curves are ambiguous due to the limited resolution of the pressure–volume grid defined by the simulations. To show the contrast between liquid-state and vapour-state isotherms, ideal gas isotherms are also calculated at 6000 K for two possible sets of species yielding a bulk SiO_2 composition. Panels (b) and (c) are calculations using the van der Waal's EoS, for qualitative comparison with the simulation results. Panel (b) shows how the volume of coexisting liquid and vapour at a given pressure can be found using an equal-area construction. Panel (c) shows the geometric relationship between the tielines of liquid–vapour coexistence, the coexistence curve representing the edge of the 'vapour dome', and the spinodal curve. (This and following figures are shown in colour in the web version of this article.)

arises because the atomic system is some orders of magnitude too small to undergo genuine liquid–vapour phase separation. The simulations constrain the position of the critical point to the region 5000–6000 K, 100–200 Å (500–1000 kg m^{-3}) and 2–5 kbar.

The pressures of isotherms at 2237 kg m^{-3} (Fig. 1a) agree to within 30% with those reported by Trave et al. (2002) and Karki et al. (2007) for liquid of comparable density. The findings are also consistent with the lower-density study of Karki et al. (2013), which presents simulations along a temperature-density (T–ρ) trajectory between 3000 K, 2180 kg m^{-3} and 8000 K, 780 kg m^{-3}; however, in that work pressure is constrained only to $P = 0 \pm 10$ kbar, so the results of the two studies cannot be compared in detail. The pressures of Karki et al. (2007, 2013) were adjusted upwards by 15 kbar in an effort to correct for the overbinding tendency of the LDA approximation, whereas Trave et al. (2002) reported uncorrected pressures, which therefore reflect the underbinding tendency of the GGA approximation. In the absence of experimental evidence, the difference between DFT studies gives a sense of the systematic uncertainties inherent in FPMD. However, in the present study, which accesses extremely low densities, the uncertainties are likely to be a strong function of volume. The weak bonding associated with GGA grows less significant as the liquid becomes more compressible ($-(\partial P/\partial V)_T$ decreases). Our simulation using LDA, at 1400 kg m^{-3} (71.3 Å), 6000 K (nominal) and −0.1 kbar, is 12 kbar below our equivalent GGA run, smaller than the +15 kbar correction adopted by Karki et al. (2007) for LDA. The LDA run also highlights the uncertainties in the critical conditions as estimated from the simulations. The 6000 K isotherm appears to be supercritical in the GGA simulations, but reaches $P = 0$ in the LDA simulations. The critical temperature T_{crit} in the LDA bulk system must be higher than in the GGA system, while P_{crit} and ρ_{crit} might be somewhat lower. Based on this discussion and our interpretation of the isotherm geometry (Fig. 1), it appears that uncertainties on the critical conditions due to the limit of resolution in the simulations are of the order of 1 kbar and some hundreds of kelvin, while uncertainty in the exchange-correlational functional might double these values.

4. Structural properties

Near its ambient-pressure melting point, silica fluid is well known to be a polymerised liquid, its nanostructure dominated by the corner-sharing tetrahedral $[SiO_4]^{2-}$ units familiar from the crystalline polymorphs. The simulated liquid in run 2237_40 (2237 kg m^{-3} or 44.6 Å, 4000 K; Table S1) meets this description, in agreement with the simulations of Karki et al. (2007). Radial distribution functions, $g(r)$, for the 2237_40 simulation show a pronounced peak in $g(r)^{Si–O}$, representing Si–O nearest neighbours, at a characteristic bond length of 1.62 Å (Fig. 2a). This peak is followed by peaks in $g(r)^{O–O}$ and $g(r)^{Si–Si}$, after which $g(r)^{O–O}$ and $g(r)^{Si–Si}$ continue approximately in anti-phase with $g(r)^{Si–O}$. The predominance of $[SiO_4]^{2-}$ tetrahedra is expressed in the fourfold coordination of Si by O and twofold coordination of O by Si (Fig. 3a).

As the temperature rises, the three-dimensional network persists in the 2237 kg m^{-3} liquid, but becomes increasingly disordered. The higher-temperature network (Fig. 3b–c) is characterised by smaller rings, while a decreasing proportion of oxygens occupy pure bridging positions between two nearest-neighbour Si atoms (a Si–O–Si structure). Some of the former bridging oxygens join Si–Si–O–Si groups, reflect the increasing tendency for Si–O–Si bridges to break and reform within the network. In the radial distribution functions (Fig. 2), the first minimum in $g(r)^{Si–O}$ rises to well above zero. This indicates an increasingly dynamic structure, in which O atoms spend a significant proportion of their time in the process of swapping between Si neighbours. Short-range order breaks down beyond the second $g(r)^{Si–O}$ peak. At 6000 K, the short-radius $g(r)^{O–O}$ function becomes smeared out in advance of the first main peak, such that for a small fraction of the time, the liquid contains O–O neighbours lying closer together than Si–O neighbours.

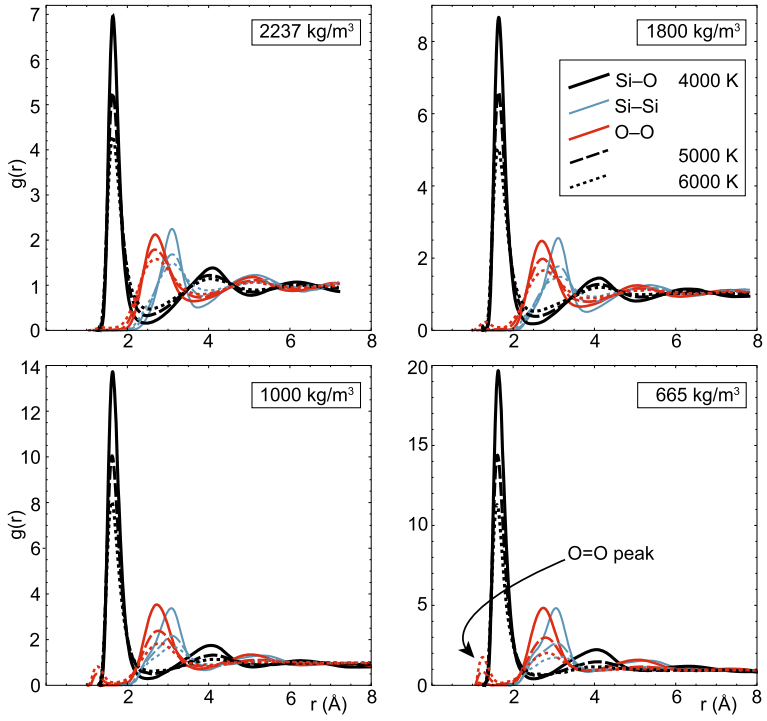

Fig. 2. Radial distribution functions (RDFs; $g(r)$) for a representative set of simulations. RDFs are shown for Si–O (black), Si–Si (blue) and O–O (red), in simulations with densities of 2237, 1800, 1000 and 665 kg m^{-3} (44.6, 55.4, 99.8 and 150.0 Å), at nominal temperatures of 4000, 5000 and 6000 K. At 2237 and 1800 kg m^{-3}, the $g(r)$ are calculated out to a radius of $r = \sqrt{2}L/2$, where L is the length of the simulation box. At 1000 and 665 kg m^{-3} the $g(r)$ are truncated at $r = 8$ Å, since at larger radii they are featureless for the highly disordered liquid. The 'O=O peak' in $g(r)^{O-O}$ is a distinctive feature of higher-temperature, lower-density simulations. It appears at a shorter radius than the dominant first Si–O peak, at a distance characteristic of the oxygen–oxygen double bond. Note the varying scales of the $g(r)$ axes. Calculated with the R.I.N.G.S. code of Le Roux and Jund (2010).

Nevertheless, each Si is still effectively coordinated to four nearest-neighbour oxygens (Fig. 3a).

As volume increases, the liquid network begins to disintegrate, developing voids (Kieffer and Angell, 1988) before being tugged into clusters. Disintegration of the network as a function of volume can be distinguished from the process of network disordering that occurs with rising temperature. Network disintegration is represented by a decrease in Si–O coordination number, which falls below 4, the value representing pervasive $[SiO_4]^{2-}$ configurations, between 1600 and 1400 kg m^{-3} (62.3–71.3 Å; Fig. 3a). Si–O and O–Si coordination numbers obtained in this study are consistent with the mean values reported by Karki et al. (2013) at 6000 K. Ultimately in the present study, Si–O coordination falls to 2.3 and O–Si coordination to 1.3, consistent with the prediction of Connolly (2016) that SiO_2-like molecules are the predominant Si-bearing species in a near-critical vapour. As the coordination numbers fall there is a corresponding decrease in characteristic ring size, and in the proportion of oxygens involved in Si–O–Si bridges (Fig. 3b–c). Radial distribution functions for low-density, high-temperature simulations show that there is essentially no short-range order beyond the initial Si–Si peaks (Fig. 2). A kink in $g(r)^{Si-Si}$ at ∼2.8 Å becomes increasingly prominent, probably reflecting the rising numbers of Si that exist on the edge of clusters and are no longer influenced symmetrically by neighbouring Si in a network. Bond and dihedral angles are discussed in Supplementary Materials.

A key feature of the simulated fluid is the formation of double-bonded oxygen pairs (O=O or O_2 in subsequent discussion) at higher volumes and temperatures. The first sign of this phenomenon is the smearing-out of the short-radius $g(r)^{O-O}$ function in the 6000 K, 2237 kg m^{-3} liquid (Fig. 2), discussed above. In lower-density simulations at 5000–6000 K, a distinct peak in $g(r)^{O-O}$ develops at a radius of 1.28 Å, characteristic of the O=O bond. The formation of such O=O pairs is symptomatic of network breakdown, leaving the pool of potentially network-forming atoms enriched in Si. At 6000 K and 665 kg m^{-3} (150 Å), 15% of oxygens in the simulation are involved in O=O pairs, such that the "bulk composition" of the remaining atoms is $X_O = O/(Si + O) = 0.63$ (Fig. 3d).

The formation of O=O pairs supports the suggestion of Iosilevskiy et al. (2014) and Connolly (2016) that by ∼1 kbar SiO_2 liquid may boil incongruently. In the case of incongruent boiling, isobaric boiling at the SiO_2 bulk composition takes place over a temperature interval, initiating with an O_2-rich vapour equilibrating with a Si-enriched liquid, with the vapour evolving up-temperature towards the system bulk composition and the liquid evolving towards a negative azeotrope on the Si-rich side of the SiO_2 bulk composition. Thus the bulk SiO_2 system of the simulations lies, from the perspective of a phase equilibrium interpretation, in the binary Si–O_2 system. The true critical point of the binary system occurs at the negative azeotrope, while the values T_{crit} and P_{crit} of the bulk SiO_2 system, referred to above, strictly represent a max condentherm and max condenbar (Connolly, 2016). At 0.001 kbar, by contrast, it has been assumed in thermodynamic analysis (e.g. Schnurre et al., 2004) that boiling does not deviate significantly from congruence.

5. Thermodynamic bulk properties and response functions

Thermodynamic bulk properties derived from the simulations are usefully considered within a wider survey of the silica fluid field. The analysis below neglects the likelihood of slightly incongruent boiling at near-critical conditions, since the thermodynamic consequences are likely small, and could not be inferred from the available data. It treats the hydrocode equation of state of Melosh (2007), termed the M-ANEOS, as representing the current understanding of SiO_2 thermodynamic properties from a planetary mod-

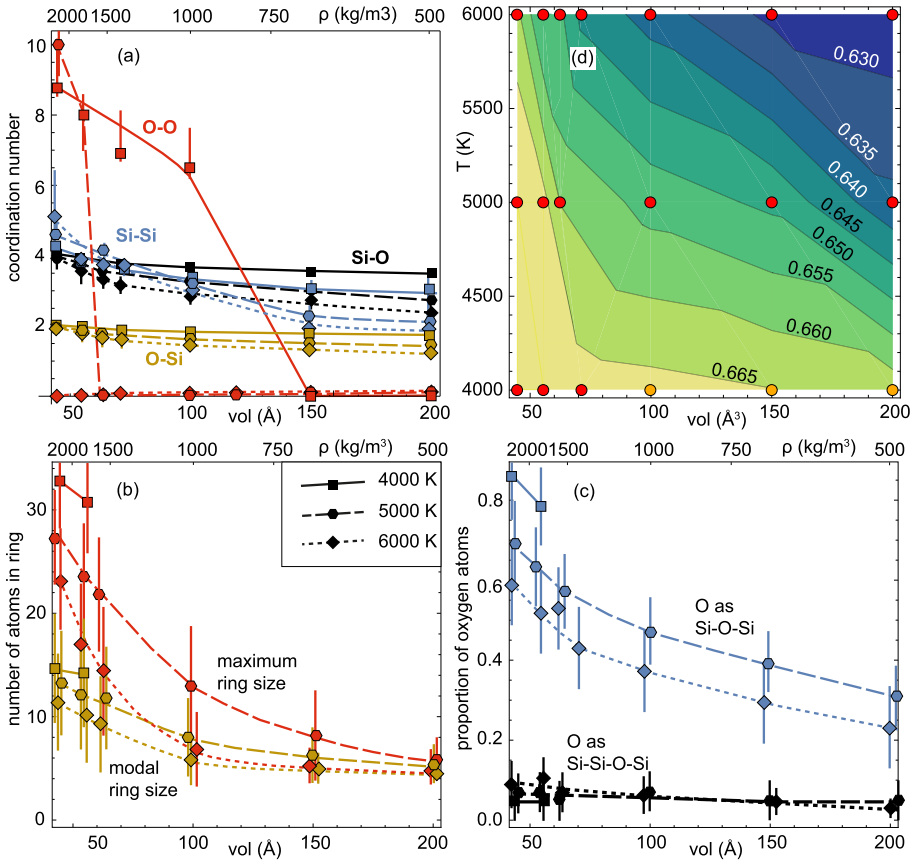

Fig. 3. Structural features of the simulated silica fluid, as a function of volume (also shown as density, ρ) and nominal temperature (4000 K: squares, solid curves; 5000 K: hexagons, dashed curves; 6000 K: diamonds, dotted curves). (a) Coordination numbers (O–O: red; Si–Si: blue; Si–O: black; O–Si: yellow), calculated with the R.I.N.G.S. code of Le Roux and Jund (2010). Because the coordination number X–Y was calculated by integrating the number of Y atoms under the first peak in the X–Y radial distribution function, the O–O coordination number plunges after the appearance of the 'O=O peak'. (b)–(c) Characteristic network topology and defects. Panel (b) shows modal (yellow) and maximum (red) ring size neglecting 3-rings, calculated with the Travis code (Brehm and Kirchner, 2011). (c) Modal proportions of O atoms occupying specific 1-oxygen local environments. Oxygens in Si–O–Si configuration (blue) form bridges between exactly two neighbouring Si atoms, while oxygens in Si–Si–O–Si environments (black) broadly provide a bridging function, but with three Si nearest neighbours in a transient configuration. The cutoff for determining nearest neighbours is the first minimum in the $g(r)^{\mathrm{Si-O}}$ or $g(r)^{\mathrm{O-O}}$ curve, discounting any initial O=O peak. (d) Average composition of the simulated fluid, excluding O=O pairs. The composition is expressed as $X_{\mathrm{O}} = \frac{\mathrm{O}}{\mathrm{Si+O}}$ for the fluid with O=O excluded, such that $X_{\mathrm{O}} = \frac{2}{3}$ for SiO_2 liquid with no O=O pairs present. Simulation conditions are represented by red dots (completed simulations) or orange dots (no production run).

elling perspective. Key properties are examined in temperature–density (T–ρ) space.

Pressure, P, has been explored across an extensive region of T–ρ space, as shown in Fig. 4a. The new simulations complement experimental and FPMD studies of the melting curve and various Hugoniot curves. In the data compilation shown, P–T coordinates and liquid and solid densities along the melting curve for $P \leq 120$ kbar were taken from the thermodynamic analysis of Holland and Powell (2011). The underlying experimental data are listed in the Supplementary Materials. Melting curve data at higher pressures were inferred from the FPMD simulations of González-Cataldo et al. (2016) and Usui and Tsuchiya (2010). The illustrated Hugoniot curves are compiled from the work of Falk et al. (2014) and Knudson and Lemke (2013) on silica aerogel, the simulations and experiments of McCoy et al. (2016b) and Qi et al. (2015) on fused silica, and the simulations of Qi et al. (2015) on "dense quartz" of super-ambient density (2940 kg m^{-3}). The FPMD study of Karki et al. (2007) straddles the melting curve, and overlaps in T–ρ space with this work.

The M-ANEOS pressure surface, shown in Fig. 4a, pre-dates much of the available data. Nevertheless it represents them well, though it tends to underestimate $(\partial P/\partial T)_\rho$ by comparison with the Hugoniot curves for fused and super-ambient density quartz, and overestimate $(\partial P/\partial \rho)_T$ by comparison with the melting curve. The version of the M-ANEOS shown in the figure is the tabulation provided by Sarah Stewart (personal communication). Fig. 4b shows the same data, overlain by a retabulated surface that matches the data somewhat better. The surface was simply extrapolated into the stability field of crystalline phases. Fig. 4c is a detail of 4b, focusing on the low-T, low-ρ portion in which the new simulations of this work outline the liquid–vapour critical region. After fitting a function to the T–ρ–P data, including the metastable and unstable simulation data, the domain of liquid–vapour coexistence was established from equal-area calculations.

The most striking deviation of observations from the M-ANEOS surface is found in the isochoric heat capacity, c_V, given by $(\partial U/\partial T)_V$. Most of the data in Fig. 5 are taken from the FPMD simulations by Karki et al. (2007) and the present work. To the FPMD data has been added a representative value of c_V, which we constructed based on unpublished data provided by F. González-Cataldo (personal communication), obtained during the study presented in González-Cataldo et al. (2016). Independent support for the FPMD data comes from the shock-wave experiments of Hicks et al. (2006). Values of c_V along the melting curve to 3000 K are also shown in Fig. 5, taken from the thermodynamic analysis of Holland and Powell (2011).

The magnitude of the c_V in the FPMD simulations is considerably higher than the values of Holland and Powell (2011) on the low-temperature melting curve, or the M-ANEOS predictions (Fig. 5a), for which c_V does not greatly exceed 3 (in dimension-

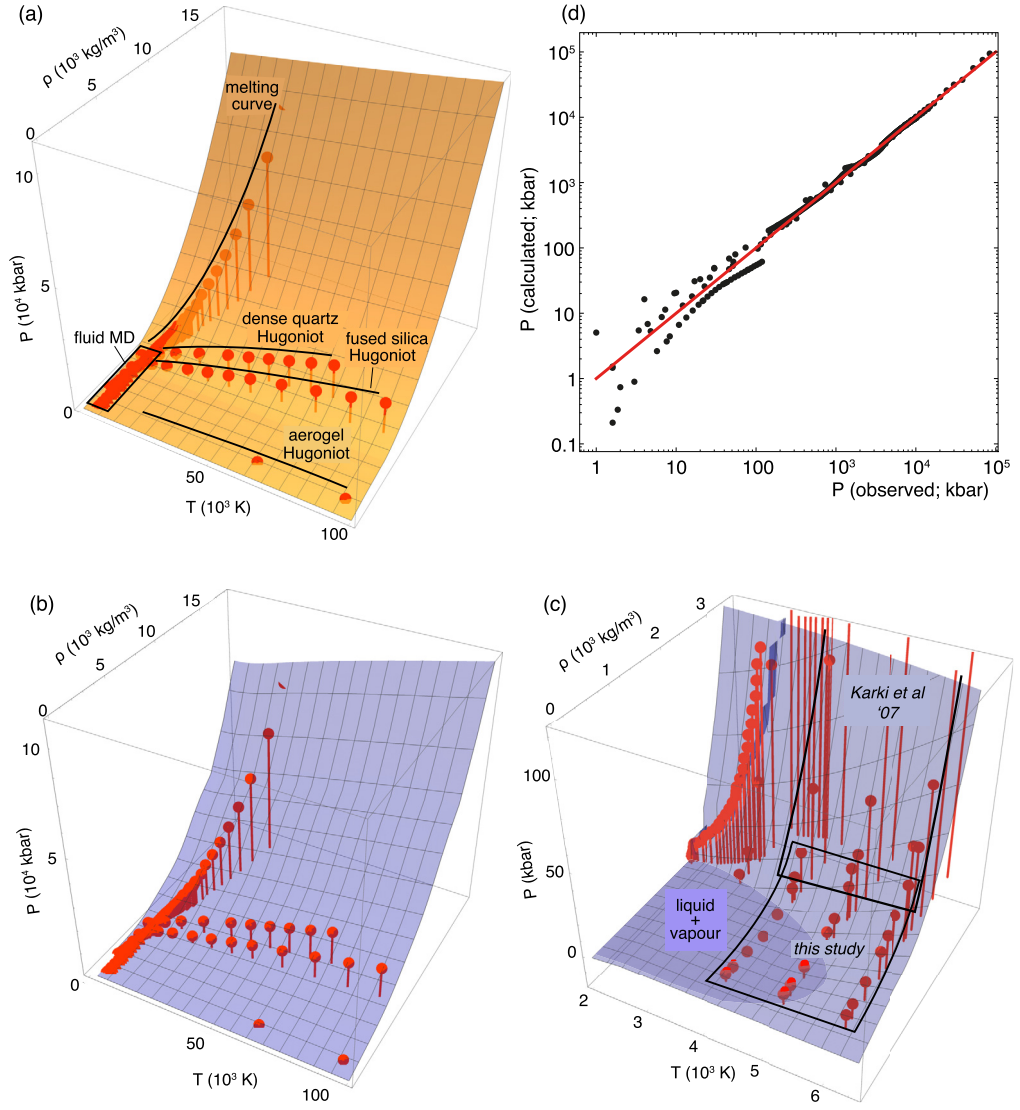

Fig. 4. Constraints on the pressure of SiO_2 fluid in temperature–density space, compared with tabulated pressure surfaces from Melosh (2007) (a) and this work (b, c). Panel (a), the M-ANEOS pressure surface, also locates the melting curve and experimental Hugoniot curves along which data were obtained. Data on the aerogel Hugoniot are from Knudson and Lemke (2013) and Falk et al. (2014); on the fused silica Hugoniot from Qi et al. (2015) and McCoy et al. (2016b); on dense quartz from Qi et al. (2015); and on the melting curve from Usui and Tsuchiya (2010), González-Cataldo et al. (2016) and Holland and Powell (2011). "Fluid MD" data are from Karki et al. (2007) and this work, as shown in (c). Panel (c) shows a detail of (b) in which the liquid–vapour coexistence region can be seen. Panel (d) plots the pressure data against values from the new pressure surface presented in this work; the 1:1 line is shown in red.

less, per-particle form) anywhere in the fluid region investigated. The M-ANEOS takes as its base value the Dulong–Petit limit of $c_V = 3$, the sum of kinetic and potential energy contributions of a harmonic oscillator that successfully approximates c_V in many crystalline solids. It then allows for an additional term accounting for speciation. However, Hicks et al. (2006) discovered a peak of $c_V \sim 5$ for silica liquid in the range 6000–35,000 K, reflecting strongly temperature-dependent depolymerisation. During this process, large c_V values are associated with a great increase in the number of ways of distributing energy over a variety of topological structures that are very similar in energy. A large anharmonic component of vibration is also present, that allows local breakup of the network as atoms pull apart from their neighbours. The peak is followed by a fall in c_V as a simpler, essentially molecular structure is attained (the "bonded liquid" of Hicks et al., 2006), and then at still higher temperatures by a further increase in c_V as the liquid approaches an atomic fluid. Given that the simulations in the present study also show extreme c_V values of 4–8 associated with depolymerisation, and considering the geometry of the proposed c_V surface (Figs. 5b–c), we believe that the high simulated heat capacities reflect the depolymerisation process.

Kraus et al. (2012) disputed the high heat capacities presented by Karki et al. (2007), citing for comparison the measurements of Richet et al. (1982) at $T \leq 1837$ K and the 3000 K DFT simulations of Ottonello et al. (2010). Kraus et al. (2012) suggested that the simulations of Karki et al. (2007) overestimate the electronic contribution to the heat capacity, c_V^{el}. In the present study, the contribution of the electronic subsystem generally accounts for less than 10% of the heat capacity. Moreover, while the electronic subsystem might plausibly make an excessive contribution to the internal energy, U, it is unclear why this would show a pronounced temperature dependence under these conditions and thereby generate a large heat capacity. Thus, we are not concerned that c_V^{el} is excessive. The simulations of Ottonello et al. (2010) were on pre-specified molecular clusters rather than an extended body of liquid that is able to explore the energy surface, while the measurements of Richet et al. (1982) were well below the temperature of depolymerisation. Heat capacities that substantially exceed the

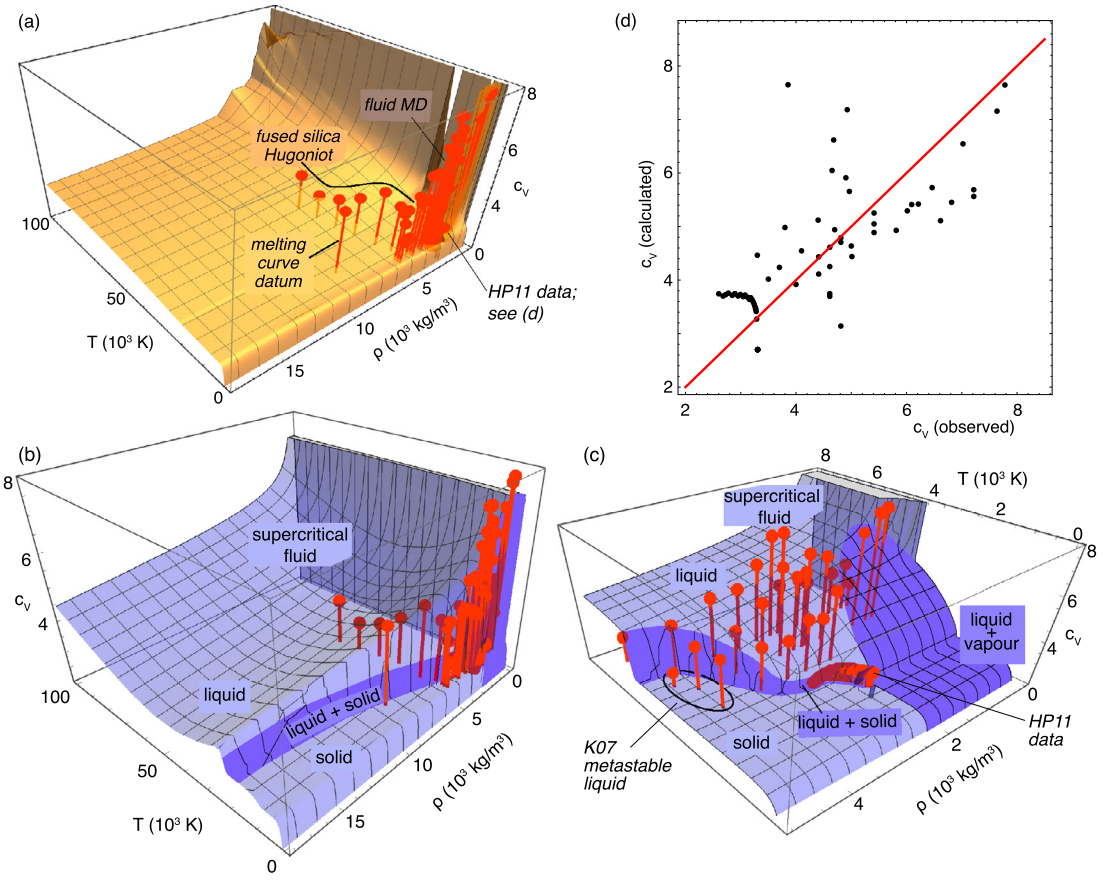

Fig. 5. Constraints on the isochoric heat capacity of SiO_2 fluid in temperature–density space, compared with tabulated heat capacity surfaces from Melosh (2007) (a) and this work (b, c). Panel (a), the M-ANEOS c_V surface, locates groups of data obtained along the fused silica Hugoniot by Hicks et al. (2006), and from fluid molecular dynamics ("fluid MD") studies on SiO_2 liquid in Karki et al. (2007) and this work. It also shows a representative datum on the melting curve, provided by F. González-Cataldo, personal communication. Panel (c) shows a detail of (b) in which the liquid–vapour coexistence region can be seen. "K07 metastable liquid": data from the simulations of Karki et al. (2007) on a liquid at below-solidus conditions. "HP11 data": values of liquid c_V along the solidus in the thermodynamic analysis of Holland and Powell (2011). Panel (d) plots the heat capacity data against values from the new c_V surface presented in this work; the 1:1 line is shown in red.

Dulong–Petit limit, due to a large anharmonic component of vibration, are familiar from other Earth materials at ~6000 K (e.g. Alfè et al., 2001).

The retabulation of the M-ANEOS SiO_2 fluid properties is described in the Supplementary Material. Among the response functions, the Grüneisen parameter, γ_V, given by $(1/\rho c_V)(\partial P/\partial T)$, is usually inferred with a large experimental uncertainty, but has recently been determined along the fused silica Hugoniot by McCoy et al. (2016a). The retabulated values match the observations well, with values lying in the range 0.6–0.8.

6. Boiling curve of silica

Fig. 6 plots the results of simulations from this work in P–T space, joined by isopycnic (equal-density) contours which intersect each other inside the two-phase region. The boiling curve and critical point were calculated based on the EoS expressions described in the previous section. Two dashed curves emanate from the boiling curve, subdividing the supercritical field: the Widom line is identified with the line of maximum c_P, while the Frenkel line marks the complete loss of oscillatory atomic motion, and is discussed in the following section. The high-temperature part of the boiling curve, and the onset of supercriticality, can be understood in terms of the depolymerisation, which is observed directly in the simulations of this work and inferred along the fused silica Hugoniot curve determined by Hicks et al. (2006). At a microstructural level, the fluid acquires supercritical properties because it is starting to undergo wholesale depolymerisation. Given that silica boiling at high temperatures is probably an incongruent process, the upper part of the "boiling curve" in Fig. 6 should strictly appear as a field.

Adopting the uncertainties on estimates of critical conditions discussed in section 3, there is essential agreement between the boiling curve inferred in this work and that of Kraus et al. (2012), with the M-ANEOS boiling curve of Melosh (2007) reaching a slightly higher critical temperature and lower critical pressure (Fig. 6). The experiments of Kraus et al. (2012) potentially constrain the boiling with more precision than the simulations, but it is difficult to assess the uncertainties in their analysis. Kraus et al. (2012) used an entropy-matching method, which requires a detailed knowledge of the entropy surface over a large region of T–ρ space. Given the apparent complexity of c_V between the fused silica Hugoniot curve and the ambient pressure liquid–vapour region, uncertainties in the results of Kraus et al. (2012) may be underestimated (see also commentary from Connolly, 2016, on the interpretation of post-decompression run products in their study).

7. Dynamic properties

The time-dependent properties of the simulated fluid give additional insight into its liquid-like versus vapour-like nature. Such properties include the velocity autocorrelation function (VACF, Fig. 7a–b), its Fourier transform the vibrational density of states (VDOS, Fig. 7c–d), and the mean-squared displacement (MSD, Fig. 8a).

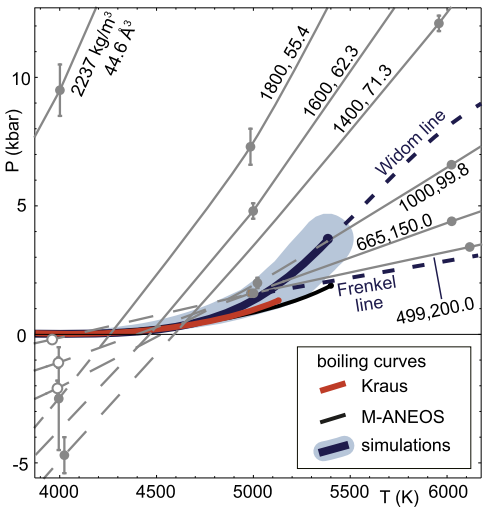

Fig. 6. Pressure, P versus true temperature, T, attained in simulations. Closed grey circles show the conditions of completed simulations, and open circles of simulations with no production run. Isopycnic contours are labelled with density ($kg\,m^{-3}$) and volume (Å). The isopycnics intersect in the two-phase coexistence region, where they are shown as dashed to indicate metastable (outside spinodal curve) or unstable (inside spinodal curve) run products. The position of the boiling curve, as calculated from the T–ρ–P surface developed in this work, is shown as a dark blue line with a representative uncertainty envelope. Positions of the Widom line (line of maximum isobaric heat capacity, calculated) and the Frenkel line at which oscillatory movement ceases (estimated from analysis of the simulations; see body text, section 7) are shown as dashed dark blue lines emanating from the simulated boiling curve. The boiling curves of Melosh (2007) and Kraus et al. (2012) are also shown.

The VACF is given by $Z(t) = \langle \vec{v}_i(0) \cdot \vec{v}_i(t) \rangle / \langle \vec{v}_i(0) \cdot \vec{v}_i(0) \rangle$, where $\vec{v}_i(t)$ is the velocity vector of atom i at time t, and VACF at successive values of t are normalised by the dot product of the first velocity vector in the trajectory with itself. In Fig. 7a–b it is averaged over 24 atoms of each element and at least 250 trajectories per atom. At lower temperature and high density, epitomised by simulation 2237_40 at 4000 K and 2237 $kg\,m^{-3}$, the VACF is characteristic of a liquid. Along a typical trajectory in this simulation, there is an initial phase of rapid decay, lasting 15 fs for Si, after which VACF oscillates while decaying slowly. This reflects the dominance of vibrations among nearest-neighbour atoms on short timescales. By ~300 fs the atomic velocity has become largely decorrelated, such that on longer timescales the trajectories become dominated by the self-diffusion of atoms. The mass-weighted VDOS, given by $\widetilde{Z}(\omega) = 2m \int_0^\infty Z(t) \cos(\omega t) dt$ (Fig. 7c–d), shows a very broad segment of the frequency spectrum occupied by periodic motion, involving stretching and bending vibrations within various geometrical settings. For simulation 2237_40, the bulk of the vibrational frequencies lie in the range 20–850 cm^{-1} for Si (950 cm^{-1} for O), encompassing vibrational periods of 35–1670 fs. The transition from the vibration-dominated to diffusion-dominated timescales is clarified in the MSD plot (Fig. 8a), where MSD is given by $\langle r(t)^2 \rangle = \frac{1}{N} \Sigma_{i=1}^{N} |\vec{r}_i(t) - \vec{r}_i(0)|^2$, $\vec{r}_i(t)$ being the position of the ith of the sample of N atoms at time t. In the first 10 fs, motion is ballistic with msd proportional to t^2 MSD, while over timescales longer than 500 fs the diffusive transport regime is characterised by MSD proportional to t. Characteristically for liquid SiO_2, there is a complex transition between the ballistic and diffusive transport regimes. The transitional timescale includes cage motion, in which a tagged particle is temporarily trapped by its neighbours,

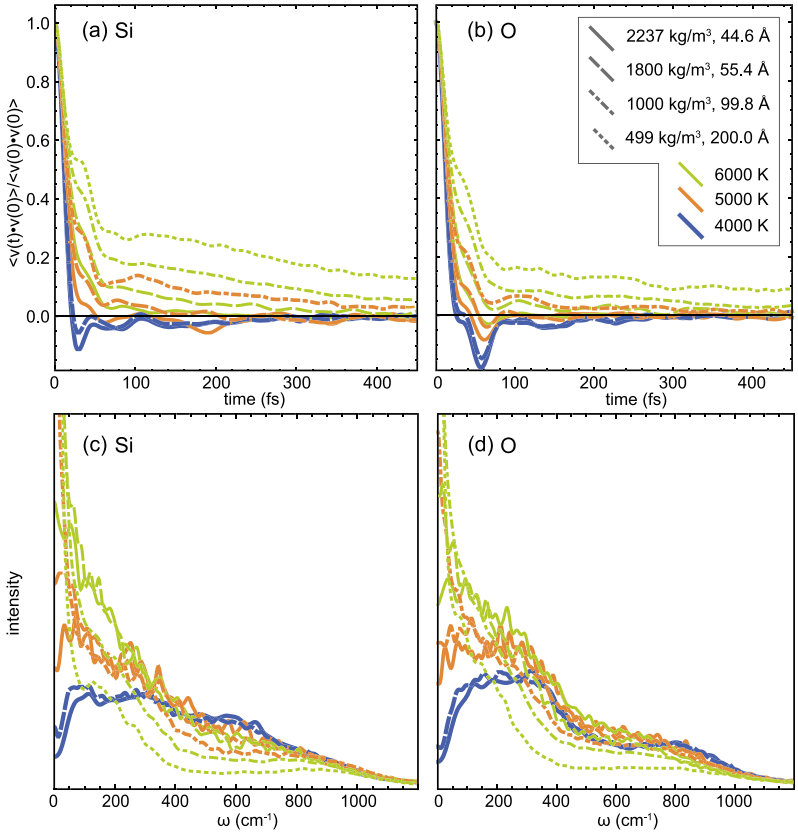

Fig. 7. Velocity-autocorrelation functions (VACF) and their corresponding frequency spectra, the vibrational density of states (VDOS), averaged over each production run, as implemented in Travis (Brehm and Kirchner, 2011). Upper panels show VACF for (a) Si and (b) O, normalised by the expected value of $v(t=0)^2$. High temperature and low density increase the tendency of the VACF to approach monotonic decay, which would represent loss of oscillatory motion of atoms and locate the Frenkel line. True monotonic decay is not attained in the simulations for Si, though it is essentially achieved for O at 6000 K and the minimum densities of 665 $kg\,m^{-3}$ and 499 $kg\,m^{-3}$. Lower panels show the mass-weighted VDOS for (c) Si and (d) O, with spectral resolutions of 2–3.5 cm^{-1}.

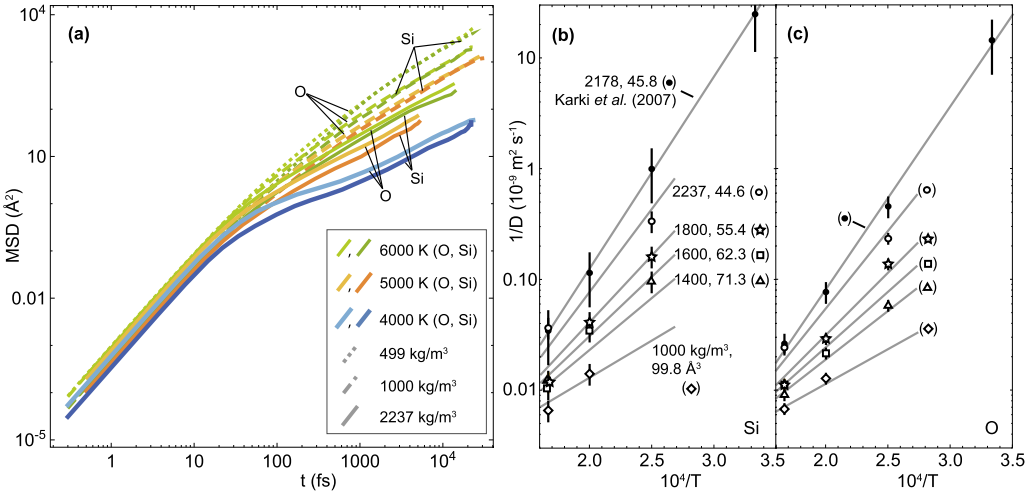

Fig. 8. (a) Mean square displacement (MSD) versus time for Si and O atoms at a variety of pressures and densities, shown on a log–log plot. Curves are shown for high density (2237 kg m^{-3} or 44.6 Å, dashed lines) and low density (1000 kg m^{-3} or 99.8 Å, solid lines), and at nominal temperature of 4000 K (blue), 5000 K (orange) and 6000 K (green). The curves for oxygen appear in a lighter shade than the equivalent curves for silicon, and are always displaced to slightly higher MSD. (b) Arrhenius plot calculated for Si atoms in the diffusive regime. Data taken from Karki et al. (2007) at 2178 kg m^{-3} is shown as closed circles. Other data are from this study, omitting run 2237_50 for which the run time was short. Isopycnic data from this work are represented with a symbol for each density as indicated, and isopycnic curves are obtained from the empirical relationship $\log(1/D) = -5.8 - 0.00163\rho + 15.4\rho/T$. The effect of pressure differences between the various runs has been neglected. (c) As (b) but for O atoms, with data from this study represented using the curves $\log(1/D) = -5.7 - 0.00161\rho + 14.4\rho/T$.

and the still poorly-understood "boson peak" (e.g. Horbach and Kob, 1999).

In simulations at high temperature (6000 K) or low density (up to 1600 kg m^{-3}), there is a smooth transition between the initial ballistic phase of an atomic trajectory and the onset of the diffusive transport regime (Fig. 8a). Correspondingly, the VACF shows a near-monotonic decorrelation of atomic velocities, and the VDOS spectra tend to a maximum intensity at 0 cm^{-1} as the dominant wavelengths of vibration tend to infinity. This behaviour resembles a typical vapour (for which the decay of VACF would be exponential) more closely than a typical liquid, although, based on their equilibrium pressure–volume relations, the simulated systems would be best described as liquids or supercritical fluids. In a nanoscopic description, the local environment of an atom, as defined by its neighbours, evolves over the timescale of its vibration. The boundary beyond which all oscillatory motion between atoms is lost is identified as the Frenkel line, and is closely approached by O atoms in the 6000 K, 499 kg m^{-3} (200 Å) simulation. Beyond this boundary, c_V is expected to decrease as vibrational modes have effectively been lost to the fluid. Although the distribution of fluid structural features is still well-defined in a statistical sense, a particular O=O pair, for example, will survive for less than one vibrational period.

Finally we consider the strength versus fragility of the SiO_2 liquid. In its $[SiO_4]^{2-}$-dominated structure at ∼2200 kg m^{-3}, silica is well known to be a strong liquid, in common with other tetrahedrally-networked liquids such as GeO_2 (Angell and Hemmati, 2013). In a strong liquid, properties such as the self-diffusion coefficient, D, show a linear Arrhenius relationship. Barrat et al. (1997) showed that SiO_2 liquid becomes fragile at high pressures where the Si–O coordination number exceeds 4, while Horbach and Kob (1999) found that strong 2200 kg m^{-3} silica liquid becomes fragile at sufficiently high temperatures. Fig. 8b–c are Arrhenius plots of $\log(1/D)$ versus $1/T$ for Si and O. The self-diffusion coefficients D were obtained from the gradient of MSD versus time in the diffusive transport regime, using the Einstein relation $D = \lim_{x\to\infty} \langle r(t)^2 \rangle / 6t$. Estimates of D are subject to temperature-dependent finite-size effects (Horbach et al., 1996; Zhang et al., 2004), introducing a poorly-quantified uncertainty. Given the uncertainty and the small number of simulation temperatures in this study, little can be said about the departure from linearity of the Arrhenius plots. However, in Fig. 8b–c, the average gradients of $\log(1/D)$ v $1/T$ increase as a function of density, whereas in the equivalent figure of Barrat et al. (1997) the opposite trend is seen. The maximum gradient at ∼2200 kg m^{-3} in both studies almost certainly reflects the fact that liquid silica ceases to be strong as it departs from the density range in which the $[SiO_4]^{2-}$-based network is pervasive.

Angell and Hemmati (2013) suggest that strong behaviour in a liquid arises from its thermodynamic properties near an order–disorder transition. For liquid silica, Angell and Hemmati (2013) envisage a liquid–liquid transition that terminates at a critical point at its low-pressure end, with strong behaviour occurring at still lower pressures, in the one-phase region. A silica liquid–liquid transition has been sought in EPMD studies (Lascaris et al., 2014, and references therein), and is hypothesised to occur at ∼5000 K and $P > 1$ bar. In the present work, no evidence is found for such a liquid–liquid transition in the stable liquid field.

8. Discussion and conclusions

New FPMD simulations on low-density silica fluid extend over 4000–6000 K and 500–2240 kg m^{-3}, a range that incorporates the liquid–vapour critical point. The results are broadly consistent with previous assessments of the critical point, based on the of shock-and-release experiments of Kraus et al. (2012) as well as a variety of thermodynamic arguments (Connolly, 2016; Iosilevskiy et al., 2014; Melosh, 2007). Analysis of the simulations demonstrates that the onset of supercriticality is intimately associated with breakup of the liquid $[SiO_4]^{2-}$ network. Below the critical temperature at 5000–6000 K, the liquid is essentially networked, albeit with an increasingly variable network topology and proportion of defects. The fluid becomes supercritical once the lattice starts to undergo true disintegration to form a molecular liquid, a process heralded by the formation of O_2 in interstices. The shock-wave study of Hicks et al. (2006) records later stages of depolymerisation, in which, at $T > 3 \times 10^4$ K, a liquid with density ∼6000 kg m^{-3} apparently becomes an atomic fluid. It is likely appropriate to construct a line of maximum isochoric heat capacity in T–ρ space, connecting the near-critical region with the heat capacity maximum of Hicks et al. (2006). Contrary to the assumptions used in some existing equations of state, dimensionless isochoric heat

capacity probably exceeds 4 per atom across much of the stable liquid field.

By combining the results of FPMD and shock-wave studies, it is possible to map isochoric heat capacity and pressure over a wide expanse of $T-\rho$ space, and thus derive a set of thermodynamic properties for fluid of silica-composition fluid. The thermodynamic surfaces provided in this work neglect the possibility of O_2 exsolution, that is, incongruent boiling, but otherwise characterise recent experimental and molecular dynamic data. They can be used to replace the M-ANEOS surfaces of Melosh (2007) for SiO_2 fluid field, where these are used in planetary modelling. Kraus et al. (2012) note that an underestimated heat capacity in the M-ANEOS of Melosh (2007) leads to an overestimation of temperature along the quartz Hugoniot, as too much irreversible work is partitioned to temperature relative to entropy. They outline the consequences for silicate vaporisation during planetary impact events. However, in seeking a simple analogue for silicate liquids, especially of Earth- or Moon-like composition, the Mg–Si–O system is preferable to the pure SiO_2 system. This encompasses the likely exsolution of O_2 vapour from the liquid at near-critical temperatures, and decay of the anomalous properties of SiO_2 liquid as network-modifying Mg cations are added.

Acknowledgements

We are grateful to Felipe González-Cataldo for sharing his unpublished data with us, and to Oliver Strickson for allowing us to use his driver for the SIESTA code. E.C.R. Green thanks the Theory Group at CIC nanoGUNE, San Sebastián, Spain, for their hospitality, and particularly Fabiano Corsetti for his careful explanations. The valuable comments of two anonymous reviewers and the editorial handing of Prof Frédéric Moynier are gratefully acknowledged. This work was supported by the Swiss National Science Foundation [grant numbers 2-77675-13 and 2-77177-15].

Appendix A. Supplementary material

Supplementary material related to this article can be found online at https://doi.org/10.1016/j.epsl.2018.03.015.

References

Alfè, D., Price, G.D., Gillan, M.J., 2001. Thermodynamics of hexagonal-close-packed iron under Earth's core conditions. Phys. Rev. B 64, 045123.
Angell, C.A., Hemmati, M., 2013. Glass transitions and critical points in orientationally disordered crystals and structural glassformers: ("strong" liquids are more interesting than we thought). AIP Conf. Proc. 1518, 9–17.
Barrat, J.-L., Badro, J., Gillet, P., 1997. A strong to fragile transition in a model of liquid silica. Mol. Simul. 20, 17–25.
Brehm, M., Kirchner, B., 2011. TRAVIS – a free analyzer and visualizer for Monte Carlo and molecular dynamics trajectories. J. Chem. Inf. Model. 51, 2007–2023.
Connolly, J.A.D., 2016. Liquid–vapor phase relations in the Si–O system: a calorically constrained van der Waals-type model. J. Geophys. Res. 121, 1641–1666.
de Koker, N., Stixrude, L., 2009. Self-consistent thermodynamic description of silicate liquids, with application to shock melting of MgO periclase and $MgSiO_3$ perovskite. Geophys. J. Int. 178, 162–179.
Falk, K., McCoy, C.A., Fryer, C.L., Greeff, C.W., Hungerford, A.L., Montgomery, D.S., Schmidt, D.W., Sheppard, D.G., Williams, J.R., Boehly, T.R., Benage, J.F., 2014. Temperature measurements of shocked silica aerogel foam. Phys. Rev. E 90, 033107.
González-Cataldo, F., Davis, S., Gutiérrez, G., 2016. Melting curve of SiO_2 at multimegabar pressures: implications for gas giants and super-Earths. Sci. Rep. 6, 26537.
Hicks, D.G., Boehly, T.R., Celliers, P.M., Eggert, J.H., Vianello, E., Meyerhofer, D.D., Collins, G.W., 2005. Shock compression of quartz in the high-pressure fluid regime. Phys. Plasmas 12, 082702.
Hicks, D.G., Boehly, T.R., Eggert, J.H., Miller, J.E., Celliers, P.M., Collins, G.W., 2006. Dissociation of liquid silica at high pressures and temperatures. Phys. Rev. Lett. 97, 025502.
Holland, T.J.B., Powell, R., 2011. An improved and extended internally consistent thermodynamic dataset for phases of petrological interest, involving a new equation of state for solids. J. Metamorph. Geol. 29, 333–383.
Horbach, J., Kob, W., 1999. Static and dynamic properties of a viscous silica melt. Phys. Rev. B 60, 3169–3181.
Horbach, J., Kob, W., Binder, K., Angell, C.A., 1996. Finite size effects in simulations of glass dynamics. Phys. Rev. E 54, R5897–R5900.
Iosilevskiy, I., Gryaznov, V., Solovev, A., 2014. Properties of high-temperature phase diagram and critical point parameters in silica. High Temp., High Press. 43, 227–241.
Karki, B.B., Bhattarai, D.B., Stixrude, L., 2007. First-principles simulations of liquid silica: structural and dynamical behavior at high pressure. Phys. Rev. B 76, 104205.
Karki, B.B., Zhang, J., Stixrude, L., 2013. First principles viscosity and derived models for $MgO–SiO_2$ melt system at high temperature. Geophys. Res. Lett. 40, 94–99.
Kieffer, J., Angell, C.A., 1988. Generation of fractal structures by negative pressure rupturing of SiO_2 glass. J. Non-Cryst. Solids 106, 336–342.
Kim, M., Khoo, K.H., Chelikowsky, J.R., 2012. Simulating liquid and amorphous silicon dioxide using real-space pseudopotentials. Phys. Rev. B 86, 054104.
Knudson, M.D., Lemke, R.W., 2013. Shock response of low-density silica aerogel in the multi-Mbar regime. J. Appl. Phys. 114, 053510.
Kraus, R.G., Stewart, S.T., Swift, D.C., Bolme, C.A., Smith, R.F., Hamel, S., Hammel, B.D., Spaulding, D.K., Hicks, D.G., Eggert, J.H., Collins, G.W., 2012. Shock vaporization of silica and the thermodynamics of planetary impact events. J. Geophys. Res., Planets 117, E09009.
Lange, R., Carmichael, I., 1987. Densities of Fe_2O_3 liquids: new measurements and derived partial molar properties. Geochim. Cosmochim. Acta 51, 2931–2946.
Lascaris, E., Hemmati, M., Buldyrev, S.V., Stanley, H.E., Austen Angell, C., 2014. Search for a liquid–liquid critical point in models of silica. J. Chem. Phys. 140, 224502.
Le Roux, S., Jund, P., 2010. Ring statistics analysis of topological networks: new approach and application to amorphous GeS_2 and SiO_2 systems. Compos. Mater. Sci. 49, 70–83.
McCoy, C.A., Gregor, M.C., Polsin, D.N., Fratanduono, D.E., Celliers, P.M., Boehly, T.R., Meyerhofer, D.D., 2016a. Measurements of the sound velocity of shock-compressed liquid silica to 1100 GPa. J. Appl. Phys. 120, 235901.
McCoy, C.A., Gregor, M.C., Polsin, D.N., Fratanduono, D.E., Celliers, P.M., Boehly, T.R., Meyerhofer, D.D., 2016b. Shock-wave equation-of-state measurements in fused silica up to 1600 GPa. J. Appl. Phys. 119, 215901.
Melosh, H.J., 2007. A hydrocode equation of state for SiO_2. Meteorit. Planet. Sci. 42, 2079–2098.
Ottonello, G., Zuccolini, M.V., Belmonte, D., 2010. The vibrational behavior of silica clusters at the glass transition: ab initio calculations and thermodynamic implications. J. Chem. Phys. 133, 104508.
Pahlevan, K., Stevenson, D.J., Eiler, J.M., 2011. Chemical fractionation in the silicate vapor atmosphere of the Earth. Earth Planet. Sci. Lett. 301, 433–443.
Perdew, J.P., Burke, K., Ernzerhof, M., 1996. Generalized gradient approximation made simple. Phys. Rev. Lett. 77, 3865–3868.
Qi, T., Millot, M., Kraus, R.G., Root, S., Hamel, S., 2015. Optical and transport properties of dense liquid silica. Phys. Plasmas 22, 062706.
Richet, P., Bottinga, Y., Denielou, L., Petitet, J., Tequi, C., 1982. Thermodynamic properties of quartz, cristobalite and amorphous SiO_2: drop calorimetry measurements between 1000 and 1800 K and a review from 0 to 2000 K. Geochim. Cosmochim. Acta 46, 2639–2658.
Saika-Voivod, I., Sciortino, F., Grande, T., Poole, P.H., 2004. Phase diagram of silica from computer simulation. Phys. Rev. E 70, 061507.
Saika-Voivod, I., Sciortino, F., Poole, P.H., 2000. Computer simulations of liquid silica: equation of state and liquid–liquid phase transition. Phys. Rev. E 63, 011202.
Sarnthein, J., Pasquarello, A., Car, R., 1995. Structural and electronic properties of liquid and amorphous SiO_2: an ab initio molecular dynamics study. Phys. Rev. Lett. 74, 4682–4685.
Schick, H.L., 1960. A thermodynamic analysis of the high-temperature vaporization properties of silica. Chem. Rev. 60, 331–362.
Schnurre, S., Gröbner, J., Schmid-Fetzer, R., 2004. Thermodynamics and phase stability in the Si–O system. J. Non-Cryst. Solids 336, 1–25.
Soler, J.M., Artacho, E., Gale, J.D., García, A., Junquera, J., Ordejón, P., Sánchez-Portal, D., 2002. The SIESTA method for *ab initio* order-*N* materials simulation. J. Phys. Condens. Matter 14, 2745–2779.
Stebbins, J., Carmichael, I., Moret, L., 1984. Heat capacities and entropies of silicate liquids and glasses. Contrib. Mineral. Petrol. 86, 131–148.
Trave, A., Tangney, P., Scandolo, S., Pasquarello, A., Car, R., 2002. Pressure-induced structural changes in liquid SiO_2 from ab initio simulations. Phys. Rev. Lett. 89, 245504.
Usui, Y., Tsuchiya, T., 2010. Ab initio two-phase molecular dynamics on the melting curve of SiO_2. J. Earth Sci. 21, 801–810.
van Beest, B.W.H., Kramer, G.J., van Santen, R.A., 1990. Force fields for silicas and aluminophosphates based on ab initio calculations. Phys. Rev. Lett. 64, 1955–1958.
Woodcock, L.V., Angell, C.A., Cheeseman, P., 1976. Molecular dynamics studies of the vitreous state: simple ionic systems and silica. J. Chem. Phys. 65, 1565–1577.
Zhang, Y., Guo, G., Refson, K., Zhao, Y., 2004. Finite-size effect at both high and low temperatures in molecular dynamics calculations of the self-diffusion coefficient and viscosity of liquid silica. J. Phys. Condens. Matter 16, 9127.